

Quantum-enhanced Landauer erasure and storage

R. Gaudenzi^{1,*}, E. Burzuri¹, S. Maegawa², H. S. J. van der Zant¹, and F. Luis³

¹*Kavli Institute of Nanoscience, Delft University of Technology, 2600 GA, Delft, The Netherlands*

²*Graduate School of Human and Environmental Studies, Kyoto University, Kyoto 606-8501, Japan and*

³*Instituto de Ciencia de Materiales de Aragón (ICMA), C.S.I.C.-Universidad de Zaragoza, E-50009 Zaragoza, Spain*

The erasure of a bit of information encoded in a physical system is an irreversible operation bound to dissipate an amount of energy $Q = k_B T \ln 2$. As a result, work $W \geq Q$ has to be applied to the physical system to restore the erased information content²⁻⁴. This limit, called Landauer limit, sets a minimal energy dissipation inherent to any classical computation. In the pursuit of the fastest and most efficient means of computation, the ultimate challenge is to produce a memory device executing an operation as close to this limit in the shortest time possible. Here, we use a crystal of molecular nanomagnets as a spin-memory device and measure the work needed to carry out a storage operation. Exploiting a form of quantum annealing, we border the Landauer limit while preserving fast operation. Owing to the tunable and fast dynamics of this process, the performance of our device in terms of energy-time cost is orders of magnitude better than existing memory devices to date. This result suggests a way to enhance classical computations by using quantum processes.

While a computation performed with an ideal binary logic gate (e.g. NOT) has no lower energy dissipation limit^{5,6}, one carried out in a memory device does. The reason is that in the former the bit is merely *displaced* isentropically in the space of states, whereas in the latter the minimal operation comprises an entropy non-conserving erasure-storage cycle. In the *erasure* step, the bit is allowed to *explore* the two binary states and the phase space doubles with a consequent entropy increase of $\Delta S = k_B \ln 2$. A corresponding minimal dissipated heat $Q = k_B T \ln 2$, called the Landauer limit, results from this entropy change. In the *storage* step, a work $W \geq Q$ has to be applied to *reduce* the system's entropy and phase space to their initial values. In order to reach the $W = Q$ limit, *reversible* operation is required. This condition is fulfilled only when using a frictionless system in a quasi-static fashion, i.e., at timescales slower than its relaxation time τ_{rel} , so that unwanted memory and hysteresis effects are avoided. For this reason, slower (faster) operation is generally associated with a lower (higher) dissipation.

This complementarity between work and time suggests considering the product $W \cdot \tau_{rel}$ – rather than either of the two – as the figure of merit assessing the energy-time cost of a computation. On one hand, driven by the demand for speed, effort has been put in pursuing fast-switching

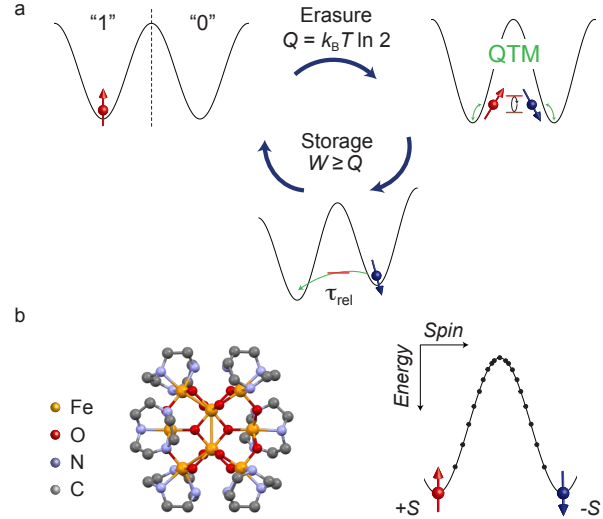


FIG. 1. **Quantum-enhanced Landauer erasure and storage of a molecular bit.** (a) Schematics of the Landauer erasure process employing a quantum nanomagnet. In order to erase the spin bit, the effective barrier separating the two binary states is lowered by inducing quantum tunneling of magnetization (QTM). A small bias magnetic field is then used to initialise the spin in the desired state within a time τ_{rel} and store the new information. The Landauer principle fixes the minimal dissipated heat Q and work W involved in the cycle. (b) Sketch of the Fe_8 easy-axis molecular magnet. In the absence of magnetic field, the double-well potential favors the two $S_z = \pm 10$ easy-axis spin eigenstates.

storage devices. This has successfully produced state-of-the-art systems with picosecond timescales, though operating far ($\gtrsim 10^6$) above the reversible limit⁷⁻¹⁰. On the other hand, reducing W down to the Landauer limit, at the expense of slow operation, has been beautifully demonstrated using small particles in traps^{11,12} or single-domain nanomagnets¹³ as envisioned by Landauer and Bennett^{1,2}.

In our experiment, a crystal of Fe_8 molecular magnets (MM) is used as a spin memory to perform a quantum-enhanced erasure-storage protocol, shown in Fig. 1(a). We encode the bit in the "up" and "down" spin states of the MM (Fig. 1(b)) and measure the magnetic susceptibility along the erasure-storage cycle. We find that the net work applied to the spin system during this cycle reaches the Landauer limit. This minimal energy cost is retained up to high operation speeds thanks to the possibility of enhancing quantum tunneling of magnetization

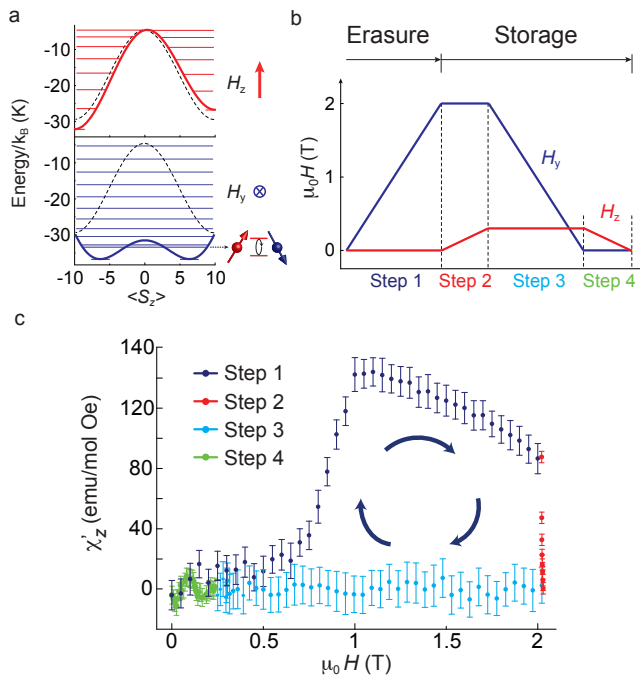


FIG. 2. **Susceptibility of the quantum MM along the erasure-storage cycle.** (a) Magnetic energy of a Fe8 MM subject to a $\mu_0 H_z = 0.2$ T longitudinal magnetic field (top) and a $\mu_0 H_y = 2$ T transverse magnetic field (bottom). Thick solid lines show the classical potential landscape while thin horizontal lines give the quantum energy levels determined by numerical diagonalisation of Eq. (1). The dotted lines show the $H = 0$ potential. While H_z introduces an energy bias between up and down spin states, thus increasing the magnetic polarization along the easy axis, H_y keeps the symmetry of the potential intact but promotes QTM between these states. (b) The 4-step sequence of magnetic fields H_y (blue) and H_z (red) constituting the erasure-storage algorithm. The first step ($H_y : 0 \rightarrow 2$ T) consists of the Landauer erasure and the remaining 3 steps correspond to the storage protocol. (c) Real component of the longitudinal magnetic ac-susceptibility, χ'_z , as a function of the vector magnetic field's modulus, measured at 1K and a frequency of 333 Hz. The sequence of steps corresponds to the one in Fig. 2(b).

(QTM) via suitably oriented external magnetic fields.

Each individual Fe₈ molecule represents a magnetic bit and is composed of eight spin- $\frac{5}{2}$ Fe³⁺-ions coupled to each other by competing antiferromagnetic interactions to form a collective $S = 10$ ($20\mu_B$) giant-spin. By bottom-up chemical synthesis, arrays of these MMs, with perfectly aligned magnetic axes, are packed into a single crystal. Due to the relatively large intermolecular spacing, the exchange interactions between the molecules are negligible¹⁴. The giant-spin $S = 10$ multiplet of the single MM is described by the following Hamiltonian¹⁵:

$$\mathcal{H} = -DS_z^2 + E(S_x^2 - S_y^2) - g\mu_B \mathbf{S} \cdot \mathbf{B}. \quad (1)$$

The ligand field, parametrised by the anisotropy constants $D = 0.294$ K and $E = 0.04$ K, defines x , y and z as the hard, medium and easy magnetic axes, re-

spectively, and creates an effective energy barrier with activation energy $U = 26.75$ K¹⁶ separating the two $S_z = \pm 10$ ground eigenstates (Fig. (1b)). The relaxation over this barrier follows approximately Arrhenius' law $\tau_{\text{rel}} = \tau_0 \exp(U/k_B T)$, where $\tau_0 = 1.43 \cdot 10^{-8}$ s is the attempt time¹⁶. The action of the magnetic field reflects into the Zeeman term of equation (1) and is depicted in Fig. 2(a), where classical potential and quantum energy levels are represented. A magnetic field parallel to the easy axis, H_z , favours either of the two eigenstates $S_z = \pm 10$, i.e., increases the "up" or "down" polarization. Instead, magnetic fields along the medium axis, H_y , give rise to off-diagonal terms that mix "up" and "down" states¹⁷. This allows the spins to tunnel through the potential barrier via progressively lower levels, thus leading to a lower effective U and a consequent decrease in τ_{rel} ¹⁵.

After aligning to the principal magnetic axes of crystal (see Appendix B), we apply the sequence of magnetic fields depicted in Fig. 2(b) – comparable to that proposed in Ref. 5 for classical magnets – in order to carry out the erasure-storage operation on our MM. In step 1, the magnetic field along the medium axis of the MM (H_y) is ramped up to 2 T and the spin states are mixed so that the bit is erased. In step 2, H_z is ramped up to 210 mT in the constant H_y field to initialise the spin in the "up" state. In steps 3 and 4, both the magnetic fields are returned to zero in the same order, closing the cycle and completing the storage.

Throughout the cycle, the complex ac-susceptibility $\chi_z = \chi'_z + i\chi''_z$ along the easy axis is measured with an inductive susceptometer (see methods for details). χ_z is proportional to the derivative of the magnetization $\partial M / \partial H_{\text{ac}}$ and is function of the temperature T , frequency ω of the ac-field H_{ac} and magnetic field vector \mathbf{H} . Measuring this quantity allows to track the dynamics of the spin system and its relaxation properties. In addition, from χ'_z the magnetization and work can be derived by integrating once and twice with respect to magnetic field. The work W obtained in this manner quantifies the heat dissipated during the erasure and measures how reversible the storage operation is^{5,13}.

The experiment is conducted at $T = 1$ K and $\omega/2\pi = 333$ Hz. This temperature is low enough to store the spins for minutes with no field applied, and high enough to have them relaxing within hundreds of nanoseconds when in a transverse field. Furthermore, at this temperature the ferromagnetic ordering can be neglected since the dipolar interaction strength is about 0.6 K¹⁴. The results for the real component of the susceptibility, χ'_z , are shown in Fig. 2(c). The susceptibility, initially zero, steeply increases at $H_y \approx 0.6$ T, reaches a peak at $H_y \approx 1$ T and slowly decreases up to $H_y = 2$ T. As a small longitudinal field is applied (step 2), χ'_z sharply drops and reaches zero at $H_z \approx 0.19$ T. Upon retracting the fields in steps 3 and 4, χ'_z remains substantially zero.

At the beginning of step 1, the spins are all blocked in either of the potential wells and the wave-function is confined to the "up" or "down" spin eigenstate. Upon

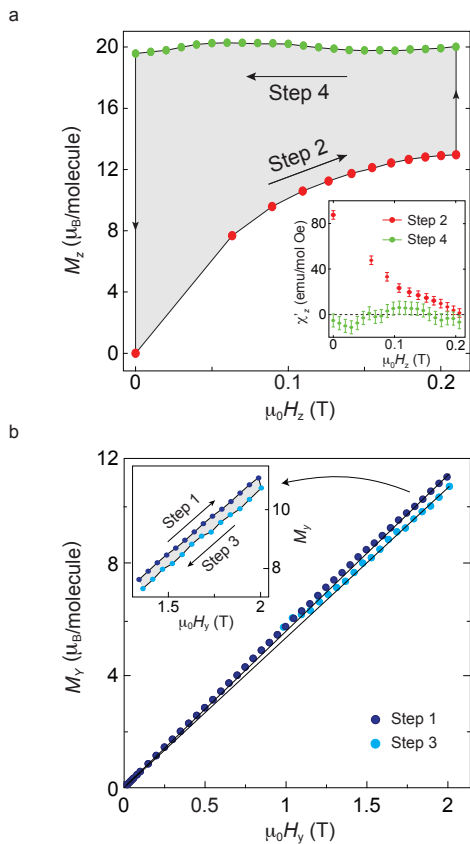


FIG. 3. **Total bit storage work.** (a) Longitudinal magnetization per molecule M_z extracted by integrating χ'_z of steps 2 and 4 (zoom-in from Fig. 2(b) in the inset) with respect to H_z . The shaded area corresponds to the work done on the system by H_z . (b) SQUID magnetization per molecule M_y along the medium axis of the MM as a function of transverse field H_y at $T = 2$ K. The slope of step 1 is higher than that of step 3 due to the small applied bias H_z field (fits are guidelines to the eye). The area enclosed by these two curves (shaded area in the inset) corresponds to the work done by H_y . This work, summed to the one in (a), yields the energy needed for storing a bit of information.

ramping up H_y , the admixture of the pure S_z eigenstates is enhanced and the wave-functions delocalised over the two potential wells¹⁸: χ'_z increases as the spin is free to tunnel between the two energetically equivalent spin states with the characteristic time τ_{rel} . In the presence of an ac-drive, the spins follow the oscillations of H_{ac} provided $\omega \lesssim 1/\tau_{\text{rel}}$. At this point, the bit is erased. In step 2, a small H_z bias magnetic field is applied. The susceptibility decreases for increasing spin polarisation reaching zero upon saturation of the magnetization. At this point, the bits are initialised in the "up" configuration. In step 3, the admixing field is ramped down and thus QTM gradually turned off. This causes the spins to remain *frozen* (i.e., out of equilibrium) in the chosen configuration upon retraction of the bias polarizing field (step 4).

By integrating the measured χ'_z with respect to H_z (inset of Fig. 3(a)), we calculate the easy axis magnetization M_z for steps 2 and 4 (see Appendix A). The result is plotted in Fig. 3(a). During step 2, M_z increases for increasing H_y before flattening out at about $13 \mu_B$. Upon retracting H_y , M_z increases up to about its maximum value of $20 \mu_B$ and remains approximately constant as H_z is also ramped to zero. The area enclosed by the magnetization loop amounts to the work made by the external magnetic field onto the molecular magnet. This yields the value $W_{2,4} \equiv W_4 - W_2 = (1.74761 \pm 0.28107) \cdot 10^{-16}$ erg/molecule, where the uncertainty corresponds to a 1σ confidence interval (see Appendix C for the determination of molecules' number and Appendix D for the uncertainties). To this quantity, the work $W_{1,3}$ done by the H_y in steps 1 and 3 needs to be added. This work cannot be extracted from the measured medium-axis susceptibility since, due to the strong magnetic anisotropy, $\chi_y (\ll \chi_z)$ is below our detection limit. However, because χ_y is approximately independent of T and ω (see Appendix B), the magnetization can be invariably measured with a SQUID at $T = 2$ K. The result is shown in Figure 3(b). The transverse magnetization M_y is recorded as H_y is ramped up to 2 T (step 1) and subsequently ramped down in the small bias longitudinal field of 0.21 T (step 3). M_y increases during step 1 and decreases, with a slightly lower slope, during step 3. The net work is given by the difference between the works W_3 and W_1 done by H_y and amounts to $W_{1,3} \equiv W_3 - W_1 = (-5.6481 \pm 1.7712) \cdot 10^{-17}$ erg/molecule. The total dissipated energy, W , is then the sum $W = W_{1,3} + W_{2,4} = (1.1828 \pm 0.3322) \cdot 10^{-16}$ erg/molecule. Within the experimental uncertainty, this is equivalent to the theoretical Landauer limit at the experimental temperature of 1 K, equal to $k_B T \ln 2 = 0.9570 \cdot 10^{-16}$ erg/bit. This proves that the present system behaves effectively like an ideal "single-spin" bit¹³.

We now discuss the extraction of the magnetic relaxation time. Ac-susceptibility measurements allow for an estimation of the dynamics of the spin relaxation processes. In particular, the ratio $\chi''_z/(\omega\chi'_z)$ measures the magnetic relaxation time τ_{rel} or, alternatively said, the time the system takes to reach equilibrium¹⁵. In Fig. 4(a) we show the evolution of τ_{rel} as a function of H_y during step 1 in the range $0.7 \leq H_y \leq 1.15$ T for which $\chi''_z \pm \sigma_{\chi''} \geq 0$ (Inset of Fig. 4(a)). We complement these data with τ_{rel} extracted from χ'_z measurements in temperature (see Appendix B). The relaxation time exponentially drops from 71.2 s at $H_y = 0$ T to $1.09 \mu\text{s}$ at $H_y = 1.7$ T. Extrapolation to $H_y = 2$ T leads to a relaxation time of 196 ns. This time is to be interpreted as the longitudinal response time of the phonon bath-and-molecule system upon a change in H_z and fixes the limit up to which quasi-static operation is retained and unwanted (dissipative) hysteresis are avoided. The product of the work and relaxation time, $W \cdot \tau_{\text{rel}}$, yields $2.31 \cdot 10^{-23}$ erg/bit-s. This figure quantifies the overall energy-time cost of a computation

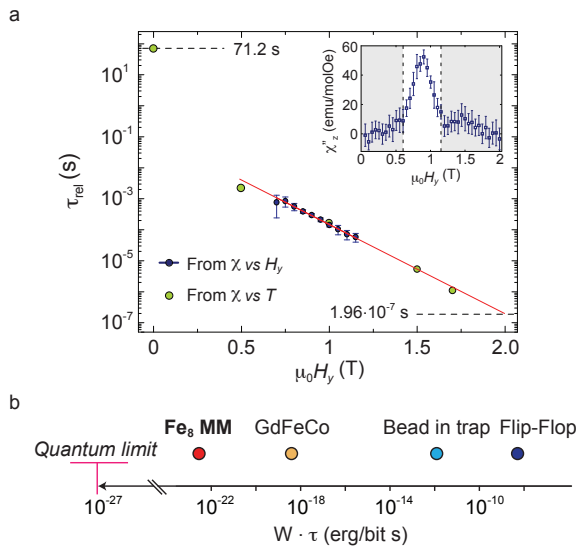


FIG. 4. Relaxation time and energy-time cost. (a) Evolution of the spin relaxation time as a function of H_y during step 1. The blue data points are obtained from χ'' in the interval $0.7 \leq H_y \leq 1.15$ T (inset). The green data points are extracted from temperature sweeps (see Appendix B). The relaxation time reaches 196 ns at $H_y = 2$ T. This value sets the maximum speed up to which quasi-static operation is retained. (b) Chart comparing the energy-time cost of a storage operation performed with various systems at their respective operating temperature. The Fe_8 in this study is the closest to the quantum limit.

and its value can be compared to that of other storage devices, operating at room temperature ($T \approx 300$ K).

As shown in Fig. 4(b) (see Appendix E for the extended chart), the product $W \cdot \tau_{\text{rel}}$ for standard flip-flops – moderately fast but lossy – is $\sim 10^{-9}$ erg/bit·s; the optical trap system in Ref. 12 – slow but efficient – attains $\sim 10^{-12}$ erg/bit·s. Increased performances ($\sim 10^{-19}$ erg/bit·s) over these two system is given by the recent GdFeCo laser-driven ferromagnetic element in Ref. 10 owing to its tens of ps operation time. The Fe_8 MM performs about 10^4 times better than this system – reducing to 100 times when accounting for the lower operating temperature. Ultimately, the product $W \cdot \tau_{\text{rel}}$ is limited by the Heisenberg uncertainty relation^{19,20}. According to it, the evolution between two orthogonal, thus classically distinguishable, bit states separated by an energy Δ would take the minimal “relaxation” time $\tau_{\text{rel}} = \pi\hbar/(2\Delta)$ called quantum speed limit^{21–23}. From it, the limit $W \cdot \tau_{\text{rel}} = \pi\hbar/2 = 1.65 \cdot 10^{-27}$ erg/bit·s is obtained as the best trade-off between speed and energy cost²⁴. Although still far from this limit, the quantum dynamics of systems like the MM in this study proves to be the key to operate both fast and at the Landauer limit and can be used to explore connection between this classical limit and the quantum speed limit.

The research reported here was supported by an advanced ERC grant (Mols@Mols). We also acknowledge financial support by the Dutch Organization for Fundamental research (NWO/FOM). EB acknowledges funds from the EU FP7 program through the project 618082 ACMOL. FL acknowledges the Spanish MINECO (grant MAT2015-68204-R), the Gobierno de Aragón (grant E98-MOLCHIP) and the European Union (COST 15128 Molecular Spintronics project). R.G. especially thanks Prof. Dr. Luca Gammaitoni for inspiring discussions.

* r.gaudenzi@tudelft.nl

- ¹ Landauer, R. Irreversibility and heat generation in the computing process. *IBM Journal of Research and Development* **5**, 183–191 (1961).
- ² Bennett, C. H. The thermodynamics of computation - a review. *International Journal of Theoretical Physics* **21**, 905–940 (1982).
- ³ Bennett, C. H. Notes on the history of reversible computation. *IBM Journal of Research and Development* **32**, 16–23 (1988).
- ⁴ Leff, H. & Rex, A. Maxwell’s demon: Information, entropy, computing. *A Hilger and Princeton Univ. Press, Europe/USA* (1990).
- ⁵ Lambson, B., Carlton, D. & Bokor, J. Exploring the thermodynamic limits of computation in integrated systems: Magnetic memory, nanomagnetic logic, and the landauer limit. *Phys. Rev. Lett.* **107**, 010604 (2011).
- ⁶ Gammaitoni, L., Chiuchiu, D., Madami, M. & Carlotti, G. Towards zero-power ict. *Nanotechnology* **26**, 222001 (2015).
- ⁷ Gerrits, T., van den Berg, H. A. M., Hohlfeld, J., Bar, L. & Rasing, T. Ultrafast precessional magnetization reversal

by picosecond magnetic field pulse shaping. *Nature* **418**, 509–512 (2002).

- ⁸ Žutić, I., Fabian, J. & Das Sarma, S. Spintronics: Fundamentals and applications. *Rev. Mod. Phys.* **76**, 323–410 (2004).
- ⁹ Ostler, T. A. *et al.* Ultrafast heating as a sufficient stimulus for magnetization reversal in a ferrimagnet. *Nature Communications* **3**, 666 (2012).
- ¹⁰ Yang, Y. *et al.* Ultrafast magnetization reversal by picosecond electrical pulses. *arXiv preprint arXiv:1609.06392* (2016).
- ¹¹ Jun, Y., Gavrilov, M. & Bechhoefer, J. High-precision test of landauer’s principle in a feedback trap. *Phys. Rev. Lett.* **113**, 190601 (2014).
- ¹² Berut, A. *et al.* Experimental verification of landauer’s principle linking information and thermodynamics. *Nature* **483**, 187–U1500 (2012).
- ¹³ Hong, J., Lambson, B., Dhuey, S. & Bokor, J. Experimental test of landauer’s principle in single-bit operations on nanomagnetic memory bits. *Science advances* **2**, 1501492 (2016).
- ¹⁴ Burzuri, E. *et al.* Magnetic dipolar ordering and quantum

- phase transition in an Fe_8 molecular magnet. *Phys. Rev. Lett.* **107**, 097203 (2011).
- ¹⁵ Gatteschi, D., Sessoli, R. & Villain, J. *Molecular nanomagnets*, vol. 5 (Oxford University Press on Demand, 2006).
- ¹⁶ Sangregorio, C., Ohm, T., Paulsen, C., Sessoli, R. & Gatteschi, D. Quantum tunneling of the magnetization in an iron cluster nanomagnet. *Phys. Rev. Lett.* **78**, 4645–4648 (1997).
- ¹⁷ Burzuri, E. *et al.* Quantum interference oscillations of the superparamagnetic blocking in an Fe_8 molecular nanomagnet. *Phys. Rev. Lett.* **111**, 057201 (2013).
- ¹⁸ Luis, F., Bartolome, J. & Fernandez, J. F. Resonant magnetic quantum tunneling through thermally activated states. *Physical Review B* **57**, 505–513 (1998).
- ¹⁹ Margolus, N. & Levitin, L. B. The maximum speed of dynamical evolution. *Physica D* **120**, 188–195 (1998).
- ²⁰ Lloyd, S. Ultimate physical limits to computation. *Nature* **406**, 1047–1054 (2000).
- ²¹ Aharonov, Y. & Bohm, D. Time in the quantum theory and the uncertainty relation for time and energy. *Phys. Rev.* **122**, 1649–1658 (1961).
- ²² Anandan, J. & Aharonov, Y. Geometry of quantum evolution. *Phys. Rev. Lett.* **65**, 1697–1700 (1990).
- ²³ Deffner, S. & Lutz, E. Energy-time uncertainty relation for driven quantum systems. *Journal of Physics a-Mathematical and Theoretical* **46** (2013).
- ²⁴ Campbell, S. & Deffner, S. Trade-off between speed and cost in shortcuts to adiabaticity. *Physical Review Letters* **118** (2017).

Appendix A: Methods

Susceptibility measurements An ac-susceptometer thermally anchored to the mixing chamber of a dilution refrigerator in combination with a 3D vector magnet (9T, 1T, 1T, 0.001° accuracy) is used to measure the erasure-storage protocol. The complex susceptibility $\chi(T, \omega) = \chi'(T, \omega) + i\chi''(T, \omega)$ is measured with a standard lock-in technique with an ac excitation magnetic field of amplitude $H_{ac} = 0.01$ Oe parallel to the common easy axis of the molecules.

Magnetization measurements Magnetization is measured with a commercial SQUID magnetometer ($T \geq 1.8$ K) equipped with a rotating stage and an ac susceptibility option.

Calculations of magnetization and work The easy-axis magnetization M_z is obtained from the susceptibility χ'_z by making use of the integral:

$$M_z = \int \chi'_z dH_z.$$

The works done by H_z (steps 2 and 4) and H_y (steps 1 and 3) are calculated by performing an analogous integration on the resulting M_z and M_y , respectively:

$$W_{2,4} = \oint M_z dH_z, \quad W_{1,3} = \oint M_y dH_y.$$

These correspond to the loop shaded areas in Fig. 3 (a) and (b).

Appendix B: Characterisation in temperature and transverse field

This section contains details on: (i) the characterisation of the superparamagnetic behaviour of the MM crystal in temperature and frequency; (ii) the extraction of the relaxation time as a function of selected H_y fields; (iii) the determination of the crystal's magnetic easy and medium axes orientation with respect to the laboratory's reference system.

(i) Temperature and frequency In Fig. B.1, the real (in-phase) $\chi'(T, \omega)$ and imaginary (out-of-phase) $\chi''(T, \omega)$ components of the ac-susceptibility are shown as a function of temperature for the indicated frequencies in zero magnetic field. For each component, the longitudinal χ_z and transverse χ_\perp parts are plotted. For a fixed frequency, decreasing the temperature results in the increase of χ'_z accompanied by a constant $\chi''_z \approx 0$. This is the typical behaviour of a standard paramagnet, where the absence of an out-of-phase response signals equilibrium and a fast relaxation time $\tau_{\text{rel}} \ll 1/\omega$. However, as a frequency-dependent temperature is reached, χ'_z starts dropping to zero while χ''_z exhibits a peak. This temperature corresponds to the so-called blocking temperature, T_b , and it is characterised by a spin relaxation time $\tau_{\text{rel}} \simeq 1/\omega$. For $T < T_b$, the spin of the MM is increasingly driven out-of-equilibrium and τ_{rel} further increases. The observed behaviour is a fingerprint of the superparamagnetism expected in a MM, where the potential barrier prevents fast spin relaxation at sufficiently low temperatures. The small temperature- and frequency-independent χ'_\perp and zero χ''_\perp further signal the strong spin polarisation along the easy-axis and negligible transverse (hard-plane) spin projection.

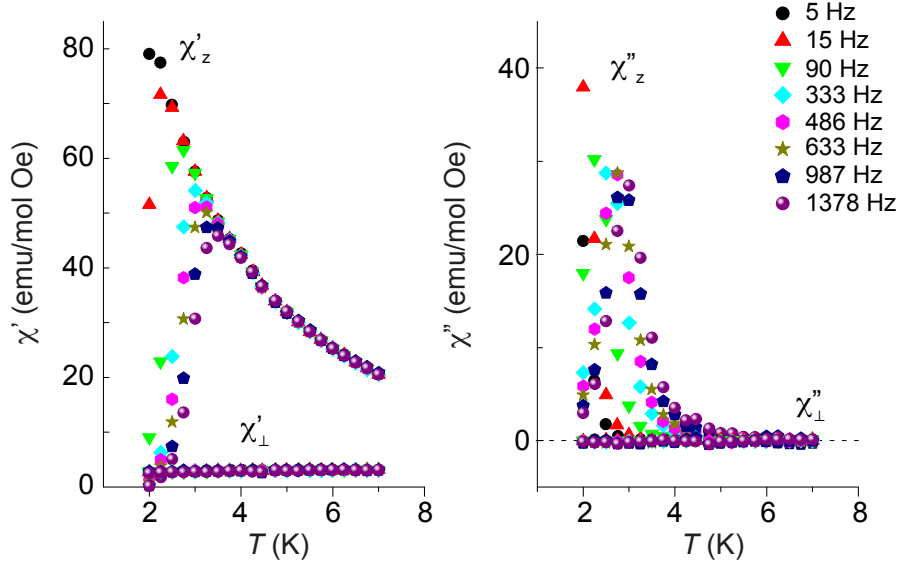


FIG. B.1. **Temperature and frequency characterization.** (a) Real (left) and imaginary (right) part of the susceptibility as a function of T and indicated frequency ω ranging from 5 Hz to 1378 Hz. The frequency-dependent departure from equilibrium signals the expected superparamagnetic behaviour.

(ii) **Transverse magnetic field** To extract the relaxation time data-points shown in Fig. 4 (and labelled " χ vs T data"), we use temperature-dependent complex susceptibility measurements for the different H_y fields at the frequency $\omega = 333$ Hz. Plotting the ratio $\chi''_z/\omega\chi'_z = \tau_{rel}$ as a function of the inverse temperature results in Fig. B.2. At high temperatures, the relaxation time behaves according to Arrhenius' law $\log \tau_{rel} = U_{eff}/T + \tau_0$ with the effective barrier $U_{eff}(H_y)$ obtained by fitting the temperature-dependent part of the curves. Extrapolation of the fit to $T = 1$ K, yields $\tau_{rel}(H_y; T = 1$ K) for the selected fields.

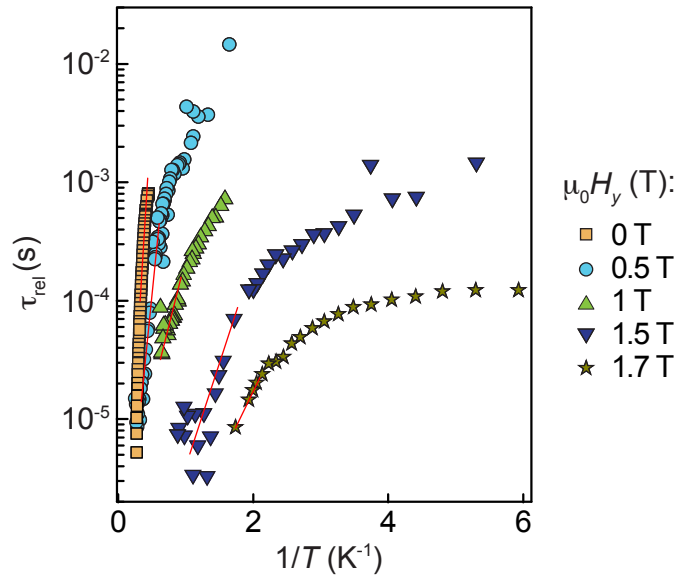


FIG. B.2. **Relaxation time for different transverse fields.** (a) τ_{rel} obtained from $\chi''_z/\omega\chi'_z$ as a function of inverse temperature. Fitting of the temperature-dependent side allows to obtain the desired $\tau_{rel}(H_y)$ at $T = 1$ K by extrapolation.

(iii) **Alignment to principal axes** In this subsection we describe the procedure used for finding the accurate orientation of the principal axes of the MM with respect to the X , Y and Z axes of the vector magnet. Provided this orientation is approximately known, the crystal is placed in the susceptometer with its easy, medium and hard

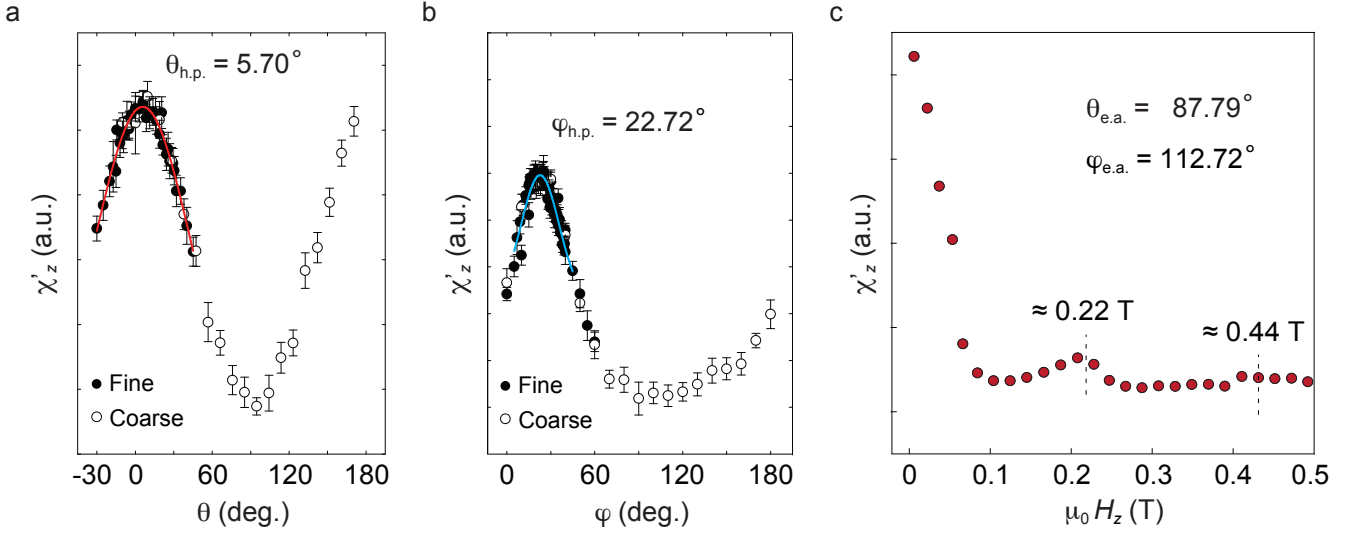


FIG. B.3. **Determination of the easy axis.** (a) χ'_z as a function of angle θ for fixed $\phi = 0^\circ$ (XZ -plane). (b) Same as (a) for fixed $\theta = 90^\circ$ (XY -plane). Maxima signal the two crossings with the hard plane from which the orientation of the easy axis is obtained. (c) χ'_z as a function of magnetic field intensity along the easy axis (labelled by the subscript z). The two peaks signal the expected magnetic level crossings.

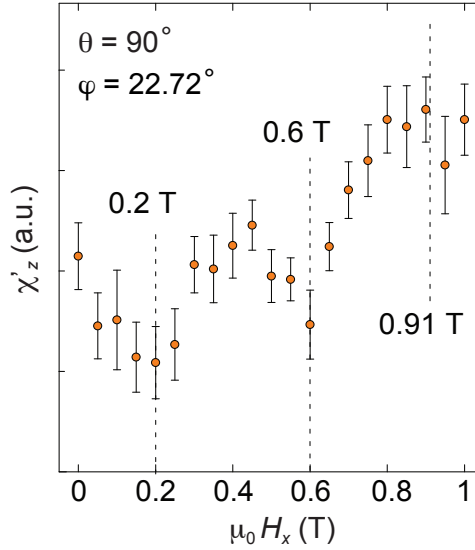


FIG. B.4. **Quantum interference pattern along the hard axis.** χ'_z as a function of magnetic field intensity along the hard axis (labelled by the subscript x). Oscillations signal the expected quantum interference pattern with minima at the indicated fields.

axes about the Y , Z and X -axis of the magnet, respectively. Measurements are executed at $T = 3$ K and $\omega = 1333$ Hz. Under these conditions, the susceptibility is close to equilibrium (see Fig. B.1) and thus strongly dependent on the magnetic field orientation. The first operation consists of rotating the magnetic field $\mu_0|H| = 0.1$ T on the XZ -plane by fixing $\phi = 0$ and sweeping θ . As Fig. B.3(a) shows, χ'_z exhibits a maximum (minimum), signalling a condition relatively closer to (further from) equilibrium. In correspondence of the maximum, for $\theta = 5.70^\circ$, the magnetic field crosses the hard plane, while it is closest to the easy axis in correspondence of the minimum. An analogous operation is conducted on the XY -plane (Fig. B.3(b)), where the crossing with the hard plane occurs for $\phi = 22.72^\circ$. The cross product between the two hard plane vectors yields an easy axis with angular coordinates $\theta = 87.79^\circ$ and $\phi = 112.72^\circ$. This axis is hereafter labelled by the subscript z . A confirmation of the accurate orientation of this axis is shown in Fig. B.3(c). Sweeping the magnetic field along it gives rise to a peak at 0.22

T (0.44 T), in correspondence of the resonance between the spin eigenstates $S_z = 10$ and $S_z = -9$ ($S_z = 10$ and $S_z = -8$) expected at $B_n = \frac{D}{g\mu_B}n = 0.219 \text{ T} \times n$, for $n = 1$ (2).

At this point, the magnetic field is swept on the hard plane for $\theta = 90^\circ$ and $\phi = 22.72^\circ$ (Fig. B.4). The observed oscillatory behaviour in χ'_z , with minima at the indicated fields, is in accordance with the characteristic quantum interference pattern (see Ref. [17] of the main text) occurring in the proximity to the hard axis – labelled by x hereafter. A 90° -shift from this axis along the hard plane fixes the medium axis – labelled by y – and concludes the orientation procedure.

Appendix C: Determination of the number of molecules

We have determined the number of molecules (bits) in the crystal with two independent methods. The first and most straightforward is that of dividing the weight of the crystal, $m = 0.411 \text{ mg}$, by the molecular weight, $P_m = 2262.45 \text{ g/mol}$ and multiply by the Avogadro constant. This yields a number of molecules $N = 1.094 \cdot 10^{17}$. The second method takes advantage of the fact that each molecule has a definite spin $S = 10$ ($20\mu_B$). By measuring the saturation magnetization, M_s , of the crystal in the SQUID setup and dividing by the spin of the single molecule yields:

$$N = \frac{M_s(\text{emu})}{20\mu_B} 5.1883 \cdot 10^{20} \mu_B/\text{emu}$$

Provided $M_s = (2.029 \pm 0.006) \cdot 10^{-2} \text{ emu}$ (Fig. C.5), $N = (1.09392 \pm 0.00326) \cdot 10^{17}$.

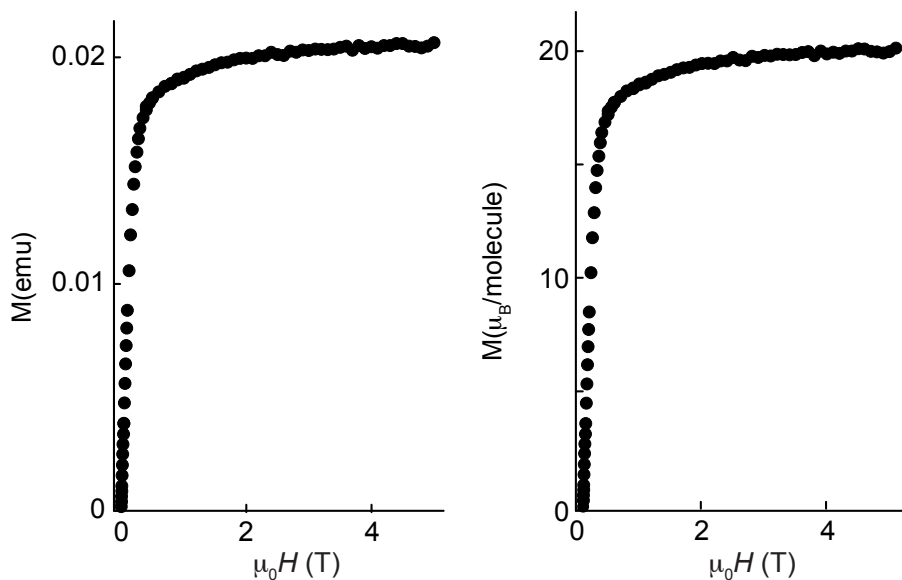


FIG. C.5. **Saturation of the magnetization.** (a) Raw magnetization M (emu) measured in the SQUID as a function of magnetic field. (b) Scaled magnetization $M(\mu_B/\text{molecule})$ obtained normalizing the raw magnetization to the single-molecule value of $20 \mu_B$. The ratio between the two quantities yields the indicated estimate for the number of molecules in the crystal.

Appendix D: Uncertainty estimation

The values of the susceptibility χ'_z given in Fig.2 at each magnetic field result from averaging over $n = 15$ samples. The uncertainty on the mean, σ_χ , is calculated as its standard deviation assuming a normal distribution. The magnetization per molecule M_z is a function of χ'_z and the number of molecules N and is therefore affected by an uncertainty $\sigma_M(H_z)$ given by the propagated uncertainties:

$$\sigma_M(H_z) = \sqrt{\left(\frac{\partial M_z}{\partial \chi'_z}\right)^2 \sigma_\chi^2 + \left(\frac{\partial M_z}{\partial N}\right)^2 \sigma_N^2}.$$

Since the work $W_{2,4}$ is calculated as:

$$W_{2,4} = \oint M_z(H_z) dH_z,$$

its upper (+) and lower (-) confidence bounds are given by:

$$W_{2,4}^{\pm} = \oint (M_z(H_z) \pm \sigma_M(H_z)) dH_z,$$

So that its associated standard deviation $\sigma_{2,4}$ is:

$$\sigma_{2,4} = |W_{2,4} - W_{2,4}^{\pm}|.$$

The uncertainty, $\sigma_{1,3}$, on the work $W_{1,3}$ – obtained by integrating M_y – is calculated using an analogous procedure.

The total error affecting the work $W = W_{1,3} + W_{2,4}$ is then $\sigma = \sqrt{\sigma_{1,3}^2 + \sigma_{2,4}^2}$.

Appendix E: Details on the energy-time cost of a computation

Here we report a more complete version of the chart in figure 4 of the main text where the quantities W and τ determining the product $W \cdot \tau$ are plotted on the Cartesian plane (Fig. E.6). Along the diagonal line, at the top-right corner of the plane sit slow and lossy devices whereas the fast and efficient ones are on the bottom-left. The devices belonging to this corner of the plane are bounded from below by the quantum limit $W \cdot \tau_{\text{rel}} = \pi \hbar / 2 = 1.65 \cdot 10^{-27}$ erg/bit·s.

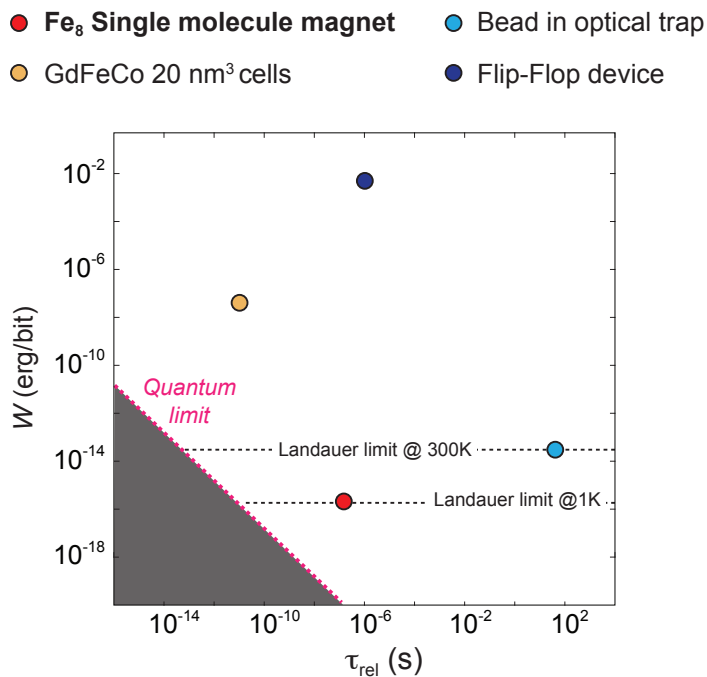


FIG. E.6. **Relaxation time and efficiency comparison.** (a) Chart comparing the energy-time cost of a storage operation performed with various systems. The Fe₈ is the closest to the quantum limit.